actuators

MDPI

Article

Disturbance Rejection for Periodic Scanning of Inertially Stabilized Platforms: An Iterative-Learning-Embedded Finite-Time Extended State Observer Approach

Chen Yue [1,2,3], Honghai Shen [1,2,3], Yongsen Xu [1,2,3], Rui Xu [1,2,3], Chao Liang [1,3] and Hairong Chu [1,2,*]

[1] Changchun Institute of Optics, Fine Mechanics and Physics, Chinese Academy of Sciences, Changchun 130033, China; yuechen21@mails.ucas.ac.cn (C.Y.); shenhh@ciomp.ac.cn (H.S.); xuyongsen@ciomp.ac.cn (Y.X.); xur@ciomp.ac.cn (R.X.); liangchao@ciomp.ac.cn (C.L.)
[2] University of Chinese Academy of Sciences, Beijing 100049, China
[3] National Key Laboratory of Dynamic Optical Imaging and Measurement, Chinese Academy of Sciences, Changchun 130033, China
* Correspondence: chuhr@ciomp.ac.cn

Abstract

During periodic scanning, friction-dominated disturbances near motion reversals cause velocity fluctuations in an inertially stabilized platform (ISP). This paper proposes a disturbance rejection control method based on an iterative-learning-embedded finite-time extended state observer (IL-FTESO). Unlike conventional external iterative learning control (ILC), which learns directly from the tracking error, the proposed method embeds ILC in the disturbance estimation channel. Within each scanning cycle, a finite-time extended state observer (FTESO) accelerates disturbance estimation, and the resulting estimate serves as the learning signal for updating the repetitive disturbance compensation in the next cycle. This structure integrates real-time disturbance estimation within each cycle with cycle-to-cycle iterative compensation. Theoretical analysis establishes convergence of the FTESO observation error and ultimate boundedness of both the learning and closed-loop tracking errors. Experiments on a physical ISP with fiber-optic gyroscope feedback show that the proposed method improves overall angular-rate tracking accuracy and suppresses error peaks near motion reversals. Compared with conventional external ILC, it reduces the root–mean–square error by 58.8% and 61.0%, the maximum absolute error by 45.4% and 48.1%, and the mean absolute error by 53.6% and 68.5% under the 20°/s, 0.5 Hz and 5°/s, 2 Hz periodic commands, respectively.

Keywords: active disturbance rejection control; inertially stabilized platform; angular-rate tracking; finite-time extended state observer; iterative learning control

Check for updates

Academic Editor: Guanghong Yang

Received: 29 August 2026
Revised: 12 October 2026
Accepted: 13 October 2026
Published: 16 October 2026

Copyright: © 2026 by the authors. Licensee MDPI, Basel, Switzerland. This article is an open access article distributed under the terms and conditions of the Creative Commons Attribution (CC BY) license.

1. Introduction

An inertially stabilized platform (ISP) is mounted on a moving carrier to isolate the optical payload from vehicle attitude disturbances. It is widely used in airborne remote sensing, target tracking, and electro-optical reconnaissance [1–3]. In practical missions, the ISP also drives the optical payload in periodic reciprocating motion for field-of-view scanning or line-of-sight tracking [4]. An inertial sensor provides angular-rate feedback to the inner control loop of the ISP servo system. The dynamic response and disturbance rejection capability of this loop directly affect angular-rate tracking accuracy during periodic scanning and, ultimately, the line-of-sight stabilization performance of the upper-level control system [5].

This inner loop, however, is subject to multiple nonlinear disturbances during periodic scanning [6], including motor cogging torque, nonlinear friction, cable drag torque, and mass imbalance [7–9]. At each velocity reversal, changes in friction direction and low-speed nonlinearities generate abrupt, nonsmooth disturbances. These disturbances induce periodic velocity fluctuations [10]. Because the scanning trajectory and reversal positions are relatively fixed, the disturbances exhibit trajectory dependence and cycle-to-cycle repeatability. The measured angular rate reflects only the motion response after the disturbances have acted on the platform. It cannot directly characterize rapid changes in the disturbances themselves. Consequently, accurately reconstructing these abrupt, nonsmooth disturbances in real time remains challenging [11–13].

Researchers have developed various control strategies to improve disturbance rejection and tracking accuracy in electro-optical platform servo systems. Owing to their structural simplicity and ease of implementation, proportional-integral-derivative (PID) control and its variants remain common. Despite these advantages, these methods generally require a tradeoff among tracking accuracy, dynamic response, and disturbance rejection performance under strong nonlinear disturbances and parameter mismatches [14,15]. Sliding mode control (SMC) has also been widely applied to servo systems because of its strong robustness against matched disturbances and parameter uncertainties, while its improved variants can further improve transient convergence performance [16–18]. However, its practical performance depends on the selection of the switching gain and the available disturbance-bound information [19]. Moreover, discontinuous switching may induce chattering, whereas continuous approximations generally introduce a tradeoff between chattering suppression and tracking accuracy. Adaptive control and friction compensation can also enhance system robustness, but their performance often depends on model information or careful parameter tuning, and their implementation may become relatively complex [20–22].

Disturbance-observer-based (DOB) control improves system robustness by estimating and compensating for model uncertainties and external disturbances [23]. In servo systems subject to periodic disturbances, adaptive periodic-disturbance observers exploit identifiable frequency characteristics to estimate harmonic disturbance components [24]. DOBs have also been combined with adaptive predefined-time control to improve transient disturbance rejection under nonlinear dynamics and actuator faults [25]. Despite these advances, model-based DOBs generally depend on a suitable nominal plant model, whereas periodic-disturbance observers often assume a harmonic disturbance structure or identifiable frequencies. Their ability to reconstruct abrupt and nonsmooth disturbances is also constrained by the available observer or filter bandwidth. Insufficient bandwidth causes attenuation and phase lag, whereas excessive bandwidth increases sensitivity to measurement noise and unmodeled high-frequency dynamics. Active disturbance rejection control (ADRC) [26,27] reduces dependence on an accurate system model by using an extended state observer (ESO) to estimate and compensate online for lumped internal and external disturbances. Nevertheless, conventional linear ESOs face the same bandwidth–noise tradeoff and may respond slowly to rapidly varying nonsmooth disturbances, including friction transients at zero-velocity crossings during motion reversals [28–30].

Recent work on faster disturbance estimation has explored cascaded, finite-time, and fixed-time ESO designs [31–33]. These structures improve observer dynamics and convergence, thereby accelerating the reconstruction of transient disturbances. Related developments include predefined-time ESOs, which allow the upper bound on the estimation-error convergence time to be specified in advance, and adaptive nonlinear ESOs, which adjust their correction gains according to the observation error to improve adaptability to varying disturbances [34,35]. In practical implementations, however, the rapid reconstruction of

abrupt, nonsmooth disturbances at velocity zero crossings remains subject to a tradeoff between transient response and noise sensitivity. Aggressive observer correction or a high effective bandwidth may amplify high-frequency gyroscope noise and exacerbate control input fluctuations [36,37]. Quasi-resonant control combined with an ESO provides another means of suppressing periodic harmonic disturbances with known frequencies and concentrated spectra. Friction at motion reversals, however, generates disturbances with abrupt local variations and broadband spectra, which cannot be adequately represented by only a few fixed resonant frequencies [38–40]. Thus, improving within-cycle observer dynamics or applying compensation at fixed resonant frequencies does not explicitly exploit the cycle-to-cycle repeatability of disturbances during periodic scanning. These limitations motivate the use of cycle-to-cycle learning.

Iterative learning control (ILC) exploits this repeatability by using tracking errors from previous cycles to update feedforward compensation at corresponding time indices in subsequent iterations [41–43]. In the periodic scanning task considered here, each complete cycle constitutes one iteration, making ILC inherently suited for suppressing trajectory-dependent repetitive disturbances [44]. Conventional ILC, however, is typically implemented as an external compensation channel that learns directly from the overall tracking error. When the measured tracking error contains measurement noise, unmodeled dynamics, or aperiodic transient disturbances, these nonrepetitive components may enter the learning update, causing compensation bias and degrading iterative convergence [45,46].

In summary, reversal disturbances during periodic scanning combine abrupt local changes with cycle-to-cycle repeatability. Existing methods have difficulty exploiting both characteristics within a unified disturbance estimation and compensation framework. Measurement noise limits the rapid reconstruction of abrupt disturbances by observers operating in real time, whereas external ILC exploits repetitive information without directly improving disturbance estimation. A framework that coordinates disturbance estimation within each cycle with cycle-to-cycle learning is therefore needed to further improve the angular-rate tracking accuracy of the ISP.

To meet this need, this paper proposes a disturbance rejection control method for the ISP pitch-axis angular-rate loop. The method uses an iterative-learning-embedded finite-time extended state observer (IL-FTESO), in which ILC is embedded in the disturbance estimation channel. Within each cycle, the FTESO estimates the residual disturbance in real time. The resulting estimate is then used to update the repetitive disturbance compensation table for the next cycle, thereby coupling within-cycle disturbance observation with cycle-to-cycle iterative learning.

The main contributions of this paper are as follows:

1. An IL-FTESO control structure is proposed that relocates the iterative-learning update from the external feedforward compensation channel used in conventional ILC [42] to the disturbance estimation channel. By learning from the residual disturbance estimate rather than the angular-rate tracking error, the proposed structure reduces reliance on observer bandwidth when rejecting repetitive disturbances with abrupt changes and limits the accumulation of aperiodic components during cycle-to-cycle learning.
2. The proposed composite closed-loop system is analyzed in terms of the convergence and boundedness of the FTESO estimation error, the ILC learning error, and the closed-loop angular-rate tracking error.
3. The proposed method is experimentally evaluated on a physical inertially stabilized platform through progressive comparisons with linear active disturbance rejection control (LADRC) [26], LADRC combined with ILC (LADRC+ILC) [42], and an IL-ESO baseline that embeds iterative learning in a linear ESO. These progressive comparisons

enable the effects of embedding iterative learning in the disturbance estimation channel and employing the finite-time observation mechanism to be evaluated separately.

The remainder of this paper is organized as follows. Section 2 presents the system modeling and problem analysis. Section 3 introduces the proposed IL-FTESO control method. Section 4 analyzes closed-loop stability. Section 5 presents the experimental results and performance comparisons. Section 6 concludes the paper.

2. Preliminaries and Problem Formulation

2.1. Dynamic Model

This study considers the pitch axis velocity loop of an inertially stabilized platform, whose mechanical structure is shown in Figure 1. A brushed dc torque motor drives the pitch axis, while a fiber-optic gyroscope (FOG) measures its angular velocity. The control objective is to achieve accurate angular-rate tracking during periodic scanning.

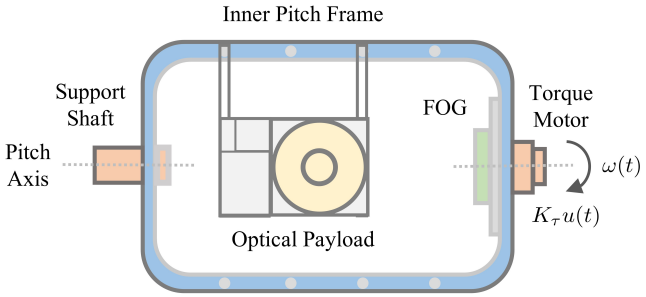


Figure 1. Structure of the ISP pitch axis.

For a precision servo system driven by a brushed DC motor, the mechanical dynamics of the velocity loop can be modeled by the following first-order differential equation:

$$J\dot{\omega}(t) + B\omega(t) = K_\tau u(t) - T_d(t), \tag{1}$$

where $\omega(t)$ is the angular velocity of the pitch axis, J is the equivalent moment of inertia, B is the viscous damping coefficient, K_τ is the equivalent gain from the control input to the electromagnetic torque, and $u(t)$ is the control input. The term $T_d(t)$ represents the equivalent disturbance torque arising from the external load, nonlinear friction, and other unmodeled disturbances. Dividing (1) by J gives

$$\dot{\omega}(t) = -\frac{B}{J}\omega(t) + bu(t) - \frac{T_d(t)}{J}. \tag{2}$$

Here, $b = K_\tau / J$ is the actual control gain. In practice, parameter identification errors, load variations, nonlinear friction, and external disturbances make accurate system parameters and disturbance models difficult to obtain. According to the basic principle of active disturbance rejection control (ADRC), parameter mismatch, unmodeled dynamics, and external disturbances can be incorporated into a lumped disturbance. Equation (2) can therefore be expressed in the standard first-order ADRC form:

$$\dot{\omega}(t) = b_0 u(t) + f(\omega, u, t), \tag{3}$$

where

$$f(\omega, u, t) = (b - b_0)u(t) - \frac{B}{J}\omega(t) - \frac{T_d(t)}{J}, \tag{4}$$

denotes the lumped disturbance comprising the control gain mismatch, unknown system dynamics, and external disturbance torque. The parameter b_0 is the nominal control gain

used by the controller and the extended state observer. Thus, the mismatch term $(b - b_0)u(t)$ between the actual gain b and its nominal value b_0 is included in the lumped disturbance for online estimation and compensation. For periodic scanning, let $k = 0, 1, 2, \ldots$ denote the scanning cycle index and let $\vartheta \in [0, T_c)$ denote the time coordinate within a cycle, where T_c is the scanning period. The continuous time t is then given by

$$t = kT_c + \vartheta. \tag{5}$$

The angular velocity, control input, disturbance torque, and lumped disturbance in the kth cycle are defined as

$$\begin{aligned} \omega_k(\vartheta) &\triangleq \omega(kT_c + \vartheta), \\ u_k(\vartheta) &\triangleq u(kT_c + \vartheta), \\ T_{d,k}(\vartheta) &\triangleq T_d(kT_c + \vartheta), \end{aligned} \tag{6}$$

and

$$f_k(\vartheta) \triangleq f\big(\omega_k(\vartheta), u_k(\vartheta), kT_c + \vartheta\big). \tag{7}$$

To explicitly account for cycle-to-cycle variations in the control input, angular-rate response, and disturbance torque, these signals are decomposed as

$$\begin{aligned} u_k(\vartheta) &= u_r(\vartheta) + \Delta u_k(\vartheta), \\ \omega_k(\vartheta) &= \omega_r(\vartheta) + \Delta\omega_k(\vartheta), \\ T_{d,k}(\vartheta) &= T_{d,r}(\vartheta) + \Delta T_{d,k}(\vartheta), \end{aligned} \tag{8}$$

where the subscript r denotes the cycle-synchronous component common to repeated executions of the same scanning task, and the corresponding incremental terms represent variations in the kth cycle. Substituting (8) into (4) gives

$$f_k(\vartheta) = f_r(\vartheta) + f_{p,k}(\vartheta), \tag{9}$$

where

$$f_r(\vartheta) = (b - b_0)u_r(\vartheta) - \frac{B}{J}\omega_r(\vartheta) - \frac{T_{d,r}(\vartheta)}{J}, \tag{10}$$

$$f_{p,k}(\vartheta) = (b - b_0)\Delta u_k(\vartheta) - \frac{B}{J}\Delta\omega_k(\vartheta) - \frac{\Delta T_{d,k}(\vartheta)}{J}. \tag{11}$$

Here, $f_r(\vartheta)$ is the repetitive disturbance component associated with the scanning trajectory, whereas $f_{p,k}(\vartheta)$ is the nonrepetitive residual component in the kth cycle. Thus, the decomposition does not require the total lumped disturbance, control input, or angular-rate response to remain identical across cycles. In particular, the cycle-to-cycle variation in the gain-mismatch term $(b - b_0)u_k(\vartheta)$ is included in $f_{p,k}(\vartheta)$.

2.2. Limitations of Conventional LADRC

For a general nth-order single-input single-output system, the input–output relationship can be written as

$$y^{(n)} = f\big(y, \dot{y}, \ldots, y^{(n-1)}, u, t\big) + b_0 u, \tag{12}$$

where y is the system output, b_0 is the nominal control gain, and $f\big(y, \dot{y}, \ldots, y^{(n-1)}, u, t\big)$ is the lumped disturbance comprising the internal dynamics, parameter uncertainties, and external disturbances.

Linear active disturbance rejection control (LADRC) treats the lumped disturbance as an extended state and estimates it online [26]. The resulting linear extended state observer (LESO) is of order $n+1$ and can be expressed as

$$\begin{cases} \dot{z}_i & = z_{i+1} + \beta_i(y - z_1), \quad i = 1, 2, \ldots, n-1, \\ \dot{z}_n & = z_{n+1} + b_0 u + \beta_n(y - z_1), \\ \dot{z}_{n+1} & = \beta_{n+1}(y - z_1). \end{cases} \tag{13}$$

Here, z_i estimates $y^{(i-1)}$ for $i = 1, 2, \ldots, n$, whereas z_{n+1} estimates the lumped disturbance $f\left(y, \dot{y}, \ldots, y^{(n-1)}, u, t\right)$.

Under bandwidth parameterization, all LESO poles are placed at $-\omega_o$, where $\omega_o > 0$ is the observer bandwidth. The characteristic polynomial of the observer error system is therefore

$$s^{n+1} + \beta_1 s^n + \cdots + \beta_n s + \beta_{n+1} = (s + \omega_o)^{n+1}. \tag{14}$$

Matching the coefficients in the binomial expansion gives

$$\beta_i = \frac{(n+1)!}{i!(n+1-i)!}\omega_o^i, \quad i = 1, 2, \ldots, n+1. \tag{15}$$

For the first-order velocity loop considered in this paper, $n = 1$, which gives $\beta_1 = 2\omega_o$ and $\beta_2 = \omega_o^2$. For notational simplicity, the lumped disturbance is denoted by $f(t)$. Assuming zero initial conditions and neglecting measurement noise, the transfer function from $f(t)$ to its estimate $z_2(t)$ is

$$\frac{Z_2(s)}{F(s)} = \frac{\beta_2}{s^2 + \beta_1 s + \beta_2} = \frac{\omega_o^2}{(s + \omega_o)^2}, \tag{16}$$

where $F(s) = \mathcal{L}\{f(t)\}$ and $Z_2(s) = \mathcal{L}\{z_2(t)\}$.

Equations (14) and (16) show that the LESO can effectively estimate constant and slowly varying disturbances. Increasing the observer bandwidth accelerates the estimation response but also heightens the LESO sensitivity to high-frequency measurement noise. Because the observer bandwidth is finite, a conventional LESO may fail to track rapidly varying nonsmooth disturbances promptly, leading to disturbance estimation lag.

2.3. Limitations of External ILC Compensation in LADRC

A common approach to exploiting the repetitive nature of periodic scanning is to combine LADRC with iterative learning control (ILC). In this configuration, ILC operates as an external learning channel and uses the tracking error to generate cycle-to-cycle compensation. The learned compensation is combined with the feedback control input and the LESO disturbance compensation term to form the final control input [42], as shown in Figure 2.

For the first-order velocity loop considered in this paper, (13) can be written explicitly as follows. For brevity, the time coordinate ϑ within each cycle is omitted from the LESO and feedback control equations:

$$\begin{cases} \dot{\hat{\omega}}_k = b_0 u_k + \hat{f}_k + \beta_1(\omega_k - \hat{\omega}_k), \\ \dot{\hat{f}}_k = \beta_2(\omega_k - \hat{\omega}_k), \\ u_k = \dfrac{\dot{\omega}_{\mathrm{ref}} + k_p(\omega_{\mathrm{ref}} - \omega_k) - \hat{f}_k}{b_0}. \end{cases} \tag{17}$$

Here, $\hat{\omega}_k$ and $\hat{f}_k$ are the angular velocity estimate and the lumped disturbance estimate, respectively, in the kth cycle.

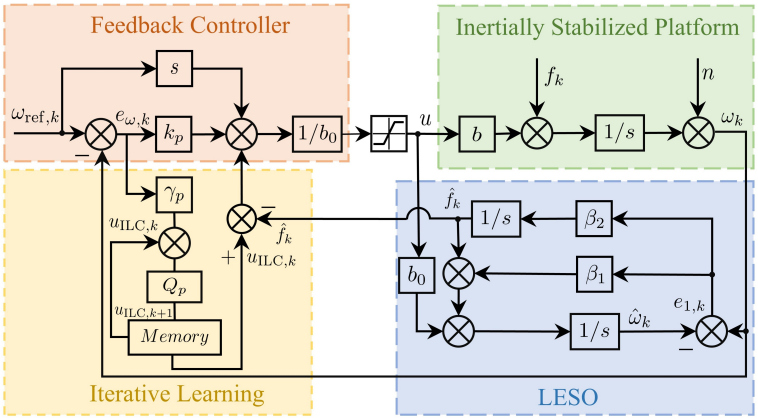


Figure 2. Block diagram of the conventional LADRC+ILC scheme.

The external ILC compensation is introduced through the control input channel. The angular-rate tracking error in the kth cycle is defined as

$$e_{\omega,k}(\vartheta) = \omega_{\mathrm{ref}}(\vartheta) - \omega_k(\vartheta), \tag{18}$$

and the control law incorporating external P-type ILC is given by

$$\begin{cases} u_k = \dfrac{\dot{\omega}_{\mathrm{ref}} + k_p e_{\omega,k} - \hat{f}_k + u_{\mathrm{ILC},k}(\vartheta)}{b_0}, \\ u_{\mathrm{ILC},k+1}(\vartheta) = Q_p\left[u_{\mathrm{ILC},k}(\vartheta) + \gamma_p e_{\omega,k}(\vartheta)\right]. \end{cases} \tag{19}$$

Here, $u_{\mathrm{ILC},k}(\vartheta)$ is the ILC compensation term, γ_p is the learning gain, and Q_p is the forgetting factor that introduces uniform attenuation in the iteration direction and limits the cycle-to-cycle accumulation of nonrepetitive components.

As shown in (19), external ILC uses the tracking error from the current cycle to update the compensation for the next cycle, thereby progressively reducing repetitive tracking errors. However, the learning update acts through the control input rather than the LESO disturbance state update and therefore does not directly improve the disturbance estimation dynamics within the current cycle. Estimation lag caused by abrupt disturbances can only be compensated gradually through feedforward learning in subsequent cycles. In addition, the angular-rate tracking error $e_{\omega,k}$ contains observer estimation residuals, measurement noise, and aperiodic disturbances; using this composite signal for learning may introduce nonrepetitive components into the learning table and degrade ILC convergence. Together, these limitations constrain the suppression of disturbance estimation lag and residual errors near abrupt disturbance transitions, even though external ILC improves periodic tracking accuracy.

3. Closed-Loop Control Algorithm Design

3.1. Design of the IL-FTESO

To improve the disturbance rejection performance of the ISP during periodic scanning, this paper proposes a disturbance rejection control method based on an iterative-learning-embedded finite-time extended state observer (IL-FTESO). During each operating cycle, the FTESO estimates in real time the residual lumped disturbance remaining after the current learned compensation is applied. At the end of the cycle, the ILC uses the resulting disturbance estimate sequence to update the periodic disturbance compensation table. The

updated compensation is applied as feedforward at the corresponding time indices in the next cycle. As the iterations proceed, trajectory-dependent repetitive disturbances are progressively learned and compensated, while the FTESO continues to estimate aperiodic disturbances and learning residuals. This architecture coordinates disturbance observation within each cycle with cycle-to-cycle iterative compensation.

Let ω_k denote the measured angular velocity during the kth operating cycle. For compactness, the argument ϑ is omitted from signals that evolve within a cycle when no ambiguity arises. The proposed IL-FTESO is formulated as

$$\begin{cases} \dot{\hat{\omega}}_k = b_0 u_k + \hat{f}_{r,k}(\vartheta) + \hat{f}_{p,k} + \zeta_1 \psi_1(e_{1,k}) \\ \dot{\hat{f}}_{p,k} = \zeta_2 \psi_2(e_{1,k}) \\ \hat{f}_{r,k+1}(\vartheta) = Q_f \left[\hat{f}_{r,k}(\vartheta) + \gamma_d \hat{f}_{p,k}(\vartheta) \right] \end{cases} \tag{20}$$

where $\hat{\omega}_k$ is the ISP angular velocity estimate; $e_{1,k} = \omega_k - \hat{\omega}_k$ is the observation error; and $\zeta_1, \zeta_2 > 0$ are constant observer gains. The term $\hat{f}_{r,k}(\vartheta)$ denotes the periodic disturbance feedforward compensation provided by the ILC at the time index ϑ within a cycle, while $\hat{f}_{p,k}$ is the FTESO estimate of the residual lumped disturbance during the current cycle. In addition, u_k is the control input in the kth cycle, b_0 is the nominal control gain, $\gamma_d > 0$ is the learning gain, and Q_f is the forgetting factor for the learning update. The block diagram of the proposed control scheme is shown in Figure 3.

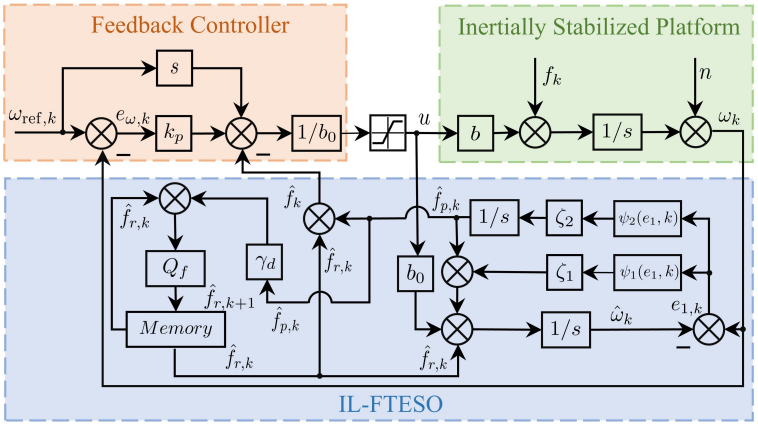


Figure 3. Block diagram of the proposed IL-FTESO control scheme.

To accelerate the estimation of the residual lumped disturbance and ensure finite-time convergence of the observation error, define the signed power function as $\lceil x \rfloor^{\alpha} \triangleq |x|^{\alpha} \operatorname{sgn}(x)$. The nonlinear correction functions $\psi_1(\cdot)$ and $\psi_2(\cdot)$ are designed as

$$\psi_1(e_{1,k}) = \lambda \lceil e_{1,k} \rfloor^{\frac{1}{2}} + e_{1,k}, \tag{21}$$

$$\psi_2(e_{1,k}) = \frac{3\lambda}{2} \lceil e_{1,k} \rfloor^{\frac{1}{2}} + \frac{\lambda^2}{2} \operatorname{sgn}(e_{1,k}) + e_{1,k}. \tag{22}$$

Here, $\lambda > 0$ is the nonlinear correction parameter. The observation error $e_{1,k}$ is used directly in deg/s without normalization. Accordingly, λ, ζ_1, and ζ_2 have units of $(\mathrm{deg/s})^{1/2}$, s^{-1}, and s^{-2}, respectively. Thus, both $\psi_1(e_{1,k})$ and $\psi_2(e_{1,k})$ have the same units as $e_{1,k}$.

For the subsequent stability analysis, define, for $e_{1,k} \neq 0$,

$$\Psi(e_{1,k}) \triangleq \frac{\partial \psi_1(e_{1,k})}{\partial e_{1,k}} = \frac{\lambda}{2} |e_{1,k}|^{-1/2} + 1.$$

It follows that

$$\psi_2(e_{1,k}) = \Psi(e_{1,k})\psi_1(e_{1,k}).$$

The linear terms maintain stable corrective action in the large-error region, whereas the fractional-power terms increase the relative correction gain as the error approaches the origin. Under the ideal signum-function assumption, this design enables the observation error to converge in finite time.

Remark 1. *The finite-time convergence analysis above assumes the ideal signum function* $\mathrm{sgn}(\cdot)$. *In the digital implementation, the signum function* $\mathrm{sgn}(e_{1,k})$ *appearing in the nonlinear correction functions is replaced by the boundary-layer saturation function*

$$\mathrm{sat}\left(\frac{e_{1,k}}{\delta}\right) = \begin{cases} \mathrm{sgn}(e_{1,k}), & |e_{1,k}| > \delta, \\ \dfrac{e_{1,k}}{\delta}, & |e_{1,k}| \le \delta, \end{cases}$$

where $\delta = 0.005\,^\circ/\mathrm{s}$ *is the boundary-layer width. The saturation approximation reduces estimation chattering caused by discontinuous switching. It coincides with the ideal signum function outside the boundary layer and provides continuous correction within it. Consequently, the observation error generally converges to a small neighborhood whose size depends on the boundary-layer width, sampling period, and measurement noise. The digital implementation should therefore be interpreted as achieving practical finite-time boundedness rather than strict finite-time convergence under the ideal signum-function assumption.*

Within the kth cycle, the total disturbance estimate for the velocity loop combines the cycle-to-cycle learned compensation with the disturbance estimate obtained in real time:

$$\hat{f}_k(\vartheta) = \hat{f}_{r,k}(\vartheta) + \hat{f}_{p,k}(\vartheta). \tag{23}$$

Remark 2. *Unlike the external ILC compensation structure defined by* (19) *and shown in Figure 2, the proposed method embeds ILC in the disturbance estimation channel. In the digital implementation, each cycle is divided into N discrete points. The cycle-to-cycle compensation table and the disturbance estimate sequence within a cycle are denoted by* $\hat{D}_{r,k} = [\hat{f}_{r,k}(1), \cdots, \hat{f}_{r,k}(N)]^{\mathrm{T}}$ *and* $\hat{F}_{p,k} = [\hat{f}_{p,k}(1), \cdots, \hat{f}_{p,k}(N)]^{\mathrm{T}}$, *respectively. At the end of each cycle, the algorithm uses* $\hat{F}_{p,k}$ *as the learning signal to update* $\hat{D}_{r,k}$, *which provides feedforward compensation during the next cycle.*

This coordinated structure offers two advantages:

1. *Repetitive trajectory-dependent abrupt disturbances are progressively compensated through the feedforward action of* $\hat{f}_{r,k}(\vartheta)$. *The FTESO therefore primarily estimates nonrepetitive disturbances and learning residuals, reducing the reliance on observer bandwidth when rejecting repetitive disturbances with abrupt changes.*
2. *The disturbance estimate* $\hat{F}_{p,k}$, *rather than the tracking error, is used as the learning signal. This choice reduces the influence of closed-loop dynamic phase lag on cycle-to-cycle learning and avoids directly introducing the composite tracking-error signal into the learning update. The forgetting factor* Q_f *introduces uniform attenuation in the iteration direction, thereby limiting the persistent cycle-to-cycle accumulation of nonrepetitive components.*

3.2. Feedback Control Law

Let $\omega_{\mathrm{ref},k}$ denote the reference angular-rate command for the ISP pitch axis during the kth operating cycle, and define the angular-rate tracking error as $e_{\omega,k} = \omega_{\mathrm{ref},k} - \omega_k$.

For notational simplicity, the time variable ϑ within each cycle is omitted throughout this subsection. From (3), the velocity error dynamics are

$$\dot{e}_{\omega,k} = \dot{\omega}_{\mathrm{ref},k} - \dot{\omega}_k = \dot{\omega}_{\mathrm{ref},k} - b_0 u_k - f_k, \tag{24}$$

where f_k is the actual lumped disturbance in the kth cycle. The composite estimate $\hat{f}_k$ in (23) is used to estimate f_k and provide feedforward disturbance compensation.

The desired velocity error dynamics are specified by the proportional feedback law

$$\dot{e}_{\omega,k} = -k_p e_{\omega,k}, \tag{25}$$

where $k_p > 0$ is the closed-loop bandwidth associated with the velocity error. Combining (24) and (25) yields

$$u_k = \frac{\dot{\omega}_{\mathrm{ref},k} + k_p e_{\omega,k} - \left[\hat{f}_{r,k} + \hat{f}_{p,k}\right]}{b_0}. \tag{26}$$

The control law comprises three components: the reference-derivative feedforward term $\dot{\omega}_{\mathrm{ref},k}$, the error feedback term $k_p e_{\omega,k}$, and the disturbance feedforward compensation term $-(\hat{f}_{r,k} + \hat{f}_{p,k})/b_0$. The disturbance estimate combines the cycle-to-cycle learned compensation $\hat{f}_{r,k}$ with the disturbance estimate $\hat{f}_{p,k}$ obtained in real time within the current cycle. The parameter k_p is typically selected such that $k_p < \omega_o$, ensuring that the observer converges faster than the feedback control response.

Define the composite disturbance compensation input $u_{d,k}$ as

$$u_{d,k} = \frac{\hat{f}_{r,k} + \hat{f}_{p,k}}{b_0}, \tag{27}$$

which represents the feedforward compensation associated with the lumped disturbance estimate produced by the IL-FTESO. In practical implementation, u_k is subject to actuator saturation to ensure that the control command remains within the linear operating ranges of the digital-to-analog converter and the voltage-controlled current source.

4. Stability Analysis

This section analyzes the stability of the proposed IL-FTESO composite control system by considering within-cycle observation and cycle-to-cycle learning. During each cycle, the learned compensation table $\hat{f}_{r,k}$ remains fixed while the FTESO estimates the residual lumped disturbance in real time. Between cycles, the ILC uses the residual disturbance estimate from the preceding cycle to update the learned compensation table for the next cycle. The analysis addresses the convergence of the FTESO observation error, the convergence of the ILC learning error, and the practical stability of the overall closed-loop system.

4.1. Within-Cycle Convergence of the FTESO

During the kth cycle, the learned compensation table $\hat{f}_{r,k}$ is treated as known and held fixed, while the FTESO estimates the residual lumped disturbance remaining after the current learned compensation is applied. For notational simplicity, the time variable ϑ within each cycle is omitted from the derivation of the observation error dynamics. From (20), the observation error system is

$$\begin{cases} \dot{e}_{1,k} = e_{2,k} - \zeta_1 \psi_1(e_{1,k}), \\ \dot{e}_{2,k} = -\zeta_2 \psi_2(e_{1,k}) + h_k. \end{cases}, \tag{28}$$

where $e_{1,k} = \omega_k - \hat{\omega}_k$ is the velocity observation error; $f_{\mathrm{res},k} = f_k - \hat{f}_{r,k}$ is the residual lumped disturbance after the learned compensation is applied in the current cycle; $e_{2,k} = f_{\mathrm{res},k} - \hat{f}_{p,k}$ is the residual disturbance estimation error; and $h_k = \dot{f}_{\mathrm{res},k}$ is the rate of change of the residual disturbance. When iterative learning compensation is not applied, setting $\hat{f}_{r,k} = 0$ allows the FTESO to estimate the original lumped disturbance f_k directly.

Assumption 1. *For any cycle k, the residual disturbance $f_{\mathrm{res},k}(\vartheta)$ may contain a finite number of jump discontinuities caused by velocity reversals. Between two adjacent jump instants, $f_{\mathrm{res},k}(\vartheta)$ is absolutely continuous with respect to ϑ, and its rate of change satisfies*

$$\left| \frac{\partial f_{\mathrm{res},k}(\vartheta)}{\partial \vartheta} \right| \leq D,$$

almost everywhere on each continuous interval, where $D > 0$ is independent of the cycle index k. In addition, the number and magnitudes of the jumps within each cycle, as well as the initial observation errors, have uniform upper bounds independent of k.

Assumption 1 ensures that the disturbance jump magnitudes are uniformly bounded with respect to k. The observation errors therefore undergo only bounded changes at the jump instants, and the errors immediately after each jump can be treated as new bounded initial conditions for the subsequent continuous interval. The following analysis is thus restricted to the continuous intervals between adjacent jump instants.

Define

$$\eta_k = \begin{bmatrix} \psi_1(e_{1,k}) \\ e_{2,k} \end{bmatrix}, \quad A = \begin{bmatrix} -\zeta_1 & 1 \\ -\zeta_2 & 0 \end{bmatrix}, \quad B = \begin{bmatrix} 0 \\ 1 \end{bmatrix}. \tag{29}$$

Because $\psi_2(e_{1,k})$ contains $\mathrm{sgn}(e_{1,k})$, the error system is discontinuous at $e_{1,k} = 0$. Solutions at this point are therefore interpreted in the Filippov sense [47,48], whereas the dynamics for $e_{1,k} \neq 0$ can be treated as ordinary differential equations. From the definition of η_k,

$$\dot{\eta}_k = \Psi(e_{1,k})(A\eta_k - B\rho_k), \tag{30}$$

where $\rho_k = -h_k(\vartheta)/\Psi(e_{1,k})$. At $e_{1,k} = 0$, the origin satisfies the Filippov equilibrium condition if $\zeta_2\lambda^2/2 > D$.

Since $|h_k(\vartheta)| \leq D$,

$$|\rho_k| \leq \frac{2D}{\lambda}|e_{1,k}|^{1/2}. \tag{31}$$

The inequality $|\psi_1(e_{1,k})| \geq \lambda|e_{1,k}|^{1/2}$ also gives $\|\eta_k\| \geq \lambda|e_{1,k}|^{1/2}$. Hence, for $L = 2D/\lambda^2$, $\rho_k^2 \leq L^2\eta_k^{\mathrm{T}}\eta_k$, or equivalently,

$$\Phi(\eta_k, \rho_k) = L^2\eta_k^{\mathrm{T}}\eta_k - \rho_k^2 \geq 0. \tag{32}$$

Theorem 1. *Suppose that Assumption 1 holds. Assume that there exist a symmetric positive definite matrix $P = P^{\mathrm{T}} \succ 0$, a constant $\kappa > 0$, and a constant $\mu \geq 0$ such that*

$$\begin{bmatrix} A^{\mathrm{T}}P + PA + \kappa P + \mu L^2 I & -PB \\ -B^{\mathrm{T}}P & -\mu \end{bmatrix} \preceq 0. \tag{33}$$

Further suppose that $\zeta_2\lambda^2/2 > D$. Over any continuous interval containing no disturbance jumps, the observation-error system is finite-time stable in the Filippov sense, with settling time T_f. If such an interval is longer than the corresponding T_f, the observation errors $(e_{1,k}, e_{2,k})$ converge to the origin before the next jump. At each bounded disturbance jump, the errors undergo only a bounded change and remain uniformly bounded with respect to the cycle index k. After the jump,

they reconverge to the origin within the corresponding T_f, provided that the subsequent continuous interval is sufficiently long.

Proof. Consider the Lyapunov function

$$V = \eta_k^{\mathrm{T}} P \eta_k. \tag{34}$$

For $e_{1,k} \neq 0$, differentiating V along the trajectories of (30) gives

$$\dot{V} = \Psi(e_{1,k}) \begin{bmatrix} \eta_k \\ \rho_k \end{bmatrix}^{\mathrm{T}} \begin{bmatrix} A^{\mathrm{T}}P + PA & -PB \\ -B^{\mathrm{T}}P & 0 \end{bmatrix} \begin{bmatrix} \eta_k \\ \rho_k \end{bmatrix}. \tag{35}$$

From (33) and the constraint $\Phi(\eta_k, \rho_k) \geq 0$,

$$\begin{bmatrix} \eta_k \\ \rho_k \end{bmatrix}^{\mathrm{T}} \begin{bmatrix} A^{\mathrm{T}}P + PA & -PB \\ -B^{\mathrm{T}}P & 0 \end{bmatrix} \begin{bmatrix} \eta_k \\ \rho_k \end{bmatrix} \leq -\kappa \eta_k^{\mathrm{T}} P \eta_k. \tag{36}$$

Substituting (36) into (35) yields

$$\dot{V} \leq -\kappa V - \frac{\kappa \lambda}{2|e_{1,k}|^{1/2}} V. \tag{37}$$

The inequality $\|\eta_k\| \geq \lambda |e_{1,k}|^{1/2}$ further gives

$$|e_{1,k}|^{1/2} \leq \frac{V^{1/2}}{\lambda \sqrt{\lambda_{\min}(P)}}. \tag{38}$$

Substitution into (37) gives

$$\dot{V} \leq -a V^{1/2} - \kappa V, \tag{39}$$

where $a = \kappa \lambda^2 \sqrt{\lambda_{\min}(P)}/2 > 0$. Equation (39) satisfies the finite-time stability criterion. Thus, over any continuous interval containing no disturbance jumps, η_k converges to zero in finite time, and the settling time satisfies

$$T_f \leq \frac{2}{\kappa} \ln\left(1 + \frac{\kappa V^{1/2}(0)}{a}\right). \tag{40}$$

Since $\eta_k = [\psi_1(e_{1,k}), e_{2,k}]^{\mathrm{T}}$, if the interval between two adjacent jump instants is longer than T_f, then $e_{1,k}$ and $e_{2,k}$ converge to zero in finite time within that interval.

At a disturbance jump instant, a bounded jump in $f_{\mathrm{res},k}$ causes a bounded change in $e_{2,k}$. Between adjacent jump instants, V decreases monotonically according to (39). Assumption 1 ensures that the initial observation errors and the quantities associated with the disturbance jumps are uniformly bounded with respect to k. Hence, there exists a constant $\bar{V} > 0$, independent of k, such that

$$V \leq \bar{V}, \qquad \forall \vartheta \in [0, T_c), \ \forall k.$$

Since $V \geq \lambda_{\min}(P) \|\eta_k\|^2$,

$$\|e_{2,k}\|_\infty \leq \varepsilon_{\mathrm{eso}}, \qquad \varepsilon_{\mathrm{eso}} \triangleq \sqrt{\frac{\bar{V}}{\lambda_{\min}(P)}}. \tag{41}$$

Therefore, the FTESO residual disturbance estimation error is uniformly bounded with respect to the cycle index k. □

A numerical feasibility check of Theorem 1 using the experimental FTESO gains is provided in Section 5.3.

4.2. Cycle-to-Cycle Convergence of the ILC

Let $\vartheta \in [0, T_c)$ denote the time coordinate within each cycle. For a bounded function $x(\vartheta)$ defined on $[0, T_c)$, define the infinity norm as

$$\|x\|_\infty \triangleq \sup_{\vartheta \in [0, T_c)} |x(\vartheta)|. \tag{42}$$

The lumped disturbance in the kth cycle is decomposed as

$$f_k(\vartheta) = f_r(\vartheta) + f_{p,k}(\vartheta), \tag{43}$$

where $f_r(\vartheta)$ is the trajectory-dependent repetitive disturbance and $f_{p,k}(\vartheta)$ is the aperiodic disturbance without consistent cycle-to-cycle repeatability. Let $\hat{f}_{r,k}(\vartheta)$ denote the learned compensation table used in the kth cycle. The residual disturbance after compensation is

$$\begin{aligned} f_{\mathrm{res},k}(\vartheta) &= f_k(\vartheta) - \hat{f}_{r,k}(\vartheta) \\ &= \tilde{f}_{r,k}(\vartheta) + f_{p,k}(\vartheta), \end{aligned} \tag{44}$$

where $\tilde{f}_{r,k}(\vartheta) = f_r(\vartheta) - \hat{f}_{r,k}(\vartheta)$ is the learning error of the repetitive disturbance component in the kth cycle.

Since $e_{2,k}(\vartheta) = f_{\mathrm{res},k}(\vartheta) - \hat{f}_{p,k}(\vartheta)$, the residual disturbance estimate used for the ILC update can be written as

$$\hat{f}_{p,k}(\vartheta) = \tilde{f}_{r,k}(\vartheta) + \Delta_k(\vartheta), \tag{45}$$

where

$$\Delta_k(\vartheta) = f_{p,k}(\vartheta) - e_{2,k}(\vartheta). \tag{46}$$

Assumption 2. *The repetitive disturbance is bounded, and the aperiodic disturbances are uniformly bounded with respect to the cycle index k. Specifically, there exist positive constants $\bar{f}_r$ and $\bar{f}_p$ such that*

$$\|f_r\|_\infty \le \bar{f}_r, \qquad \|f_{p,k}\|_\infty \le \bar{f}_p, \qquad \forall k. \tag{47}$$

Equations (41) and (46) give

$$\|\Delta_k\|_\infty \le \bar{f}_p + \varepsilon_{\mathrm{eso}} \triangleq \bar{\Delta}. \tag{48}$$

Under Assumption 1, Theorem 1 establishes a uniform observation-error bound for the ideal continuous-time model, independently of the subsequent ILC convergence analysis. In the digital implementation, measurement noise, quantization errors, and sampling errors are treated as additional bounded perturbations, and $\varepsilon_{\mathrm{eso}}$ is interpreted as the corresponding enlarged practical bound. Hence, the uniform boundedness of $\Delta_k(\vartheta)$ does not rely on the ILC convergence result.

To characterize the attenuation of the repetitive disturbance caused by the forgetting factor Q_f, define the forgetting bias as

$$\delta_Q(\vartheta) = (1 - Q_f) f_r(\vartheta), \quad \|\delta_Q\|_\infty \le (1 - Q_f)\bar{f}_r \triangleq \bar{\delta}_Q. \tag{49}$$

When $Q_f = 1$, $\bar{\delta}_Q = 0$.

Theorem 2. *Consider the ILC update law in (20). Suppose that Assumption 2 holds, $0 < Q_f \leq 1$, and the learning contraction condition*

$$\rho_L = Q_f|1 - \gamma_d| < 1 \tag{50}$$

is satisfied. Then, the repetitive disturbance learning error is ultimately bounded and satisfies

$$\limsup_{k\to\infty} \|\tilde{f}_{r,k}\|_\infty \leq \frac{\bar{\delta}_Q + \gamma_d Q_f \bar{\Delta}}{1 - \rho_L}. \tag{51}$$

In particular, when $Q_f = 1$ and $\bar{\Delta} = 0$, $\tilde{f}_{r,k}(\vartheta)$ converges to zero over successive cycles.

Proof. Substituting (45) into the ILC update law gives

$$\begin{aligned}\tilde{f}_{r,k+1}(\vartheta) &= f_r(\vartheta) - Q_f\left[\hat{f}_{r,k}(\vartheta) + \gamma_d\left(\tilde{f}_{r,k}(\vartheta) + \Delta_k(\vartheta)\right)\right] \\ &= Q_f\left[f_r(\vartheta) - \hat{f}_{r,k}(\vartheta)\right] + (1 - Q_f) f_r(\vartheta) \\ &\quad - \gamma_d Q_f \tilde{f}_{r,k}(\vartheta) - \gamma_d Q_f \Delta_k(\vartheta) \\ &= Q_f(1 - \gamma_d)\tilde{f}_{r,k}(\vartheta) + \delta_Q(\vartheta) - \gamma_d Q_f \Delta_k(\vartheta).\end{aligned} \tag{52}$$

Taking the infinity norm gives

$$\|\tilde{f}_{r,k+1}\|_\infty \leq \rho_L \|\tilde{f}_{r,k}\|_\infty + \bar{\delta}_Q + \gamma_d Q_f \bar{\Delta}. \tag{53}$$

Recursively applying this inequality yields

$$\begin{aligned}\|\tilde{f}_{r,k}\|_\infty &\leq \rho_L^k \|\tilde{f}_{r,0}\|_\infty \\ &\quad + \frac{1 - \rho_L^k}{1 - \rho_L}\left(\bar{\delta}_Q + \gamma_d Q_f \bar{\Delta}\right).\end{aligned} \tag{54}$$

Since $\rho_L < 1$, taking $k \to \infty$ gives (51). □

Remark 3. *For $0 < Q_f \leq 1$, the condition $0 < \gamma_d < 2$ is sufficient for $\rho_L < 1$. Reducing Q_f limits the cycle-to-cycle accumulation of nonrepetitive components but increases the forgetting bias $\bar{\delta}_Q$.*

Remark 4. *The ILC generates the learned compensation $\hat{f}_{r,k}(\vartheta)$ by progressively compensating for trajectory-dependent repetitive disturbances across cycles. The FTESO estimates in real time the residual disturbance $f_{\mathrm{res},k}(\vartheta)$ in (44), which contains the repetitive disturbance learning error and the aperiodic disturbance. Together, these quantities form the total disturbance estimate in (23). The resulting total disturbance estimation error is*

$$\Delta_{f,k}(\vartheta) = f_k(\vartheta) - \hat{f}_k(\vartheta) = e_{2,k}(\vartheta). \tag{55}$$

Therefore, (41) gives

$$\|\Delta_{f,k}\|_\infty = \|e_{2,k}\|_\infty \leq \varepsilon_{\mathrm{eso}}. \tag{56}$$

4.3. Practical Closed-Loop Stability

Theorem 3. *Consider the composite closed-loop system consisting of the IL-FTESO, the ILC embedded in the disturbance estimation channel, and the velocity error feedback control law. Suppose that the preceding assumptions hold and that $k_p > 0$. Further suppose that the ILC satisfies the*

contraction condition $\rho_L < 1$ *and that the FTESO residual disturbance estimation error satisfies* $\|e_{2,k}\|_\infty \le \varepsilon_{\text{eso}}$.

Then, both the repetitive disturbance learning error and the angular-rate tracking error are ultimately bounded. The steady-state tracking error over successive cycles satisfies

$$\limsup_{k\to\infty} \|e_{\omega,k}\|_\infty \le \frac{\varepsilon_{\text{eso}}}{k_p}. \tag{57}$$

Proof. The cycle-to-cycle ILC convergence analysis establishes that the repetitive disturbance learning error $\tilde{f}_{r,k}$ is ultimately bounded when $\rho_L < 1$. The within-cycle FTESO analysis further establishes that the residual disturbance estimation error is uniformly bounded with respect to k.

During the kth cycle, the learned compensation table $\hat{f}_{r,k}$ remains fixed while the FTESO estimates the residual disturbance in real time. At the end of the cycle, the resulting estimate $\hat{f}_{p,k}$ is used to update the learned compensation table for the next cycle. The update is therefore causal and introduces no algebraic loop at the same time instant.

Substituting the control law into the velocity error dynamics gives

$$\dot{e}_{\omega,k}(\vartheta) = -k_p e_{\omega,k}(\vartheta) - e_{2,k}(\vartheta). \tag{58}$$

Mapping the time coordinate ϑ within each cycle to the original time coordinate $t = kT_c + \vartheta$ and concatenating the error trajectories over successive cycles give

$$\dot{e}_\omega(t) = -k_p e_\omega(t) - e_2(t). \tag{59}$$

The solution to this first-order differential equation is

$$e_\omega(t) = e^{-k_p t} e_\omega(0) - \int_0^t e^{-k_p(t-\tau)} e_2(\tau)\,\mathrm{d}\tau. \tag{60}$$

Hence,

$$|e_\omega(t)| \le e^{-k_p t}|e_\omega(0)| + \frac{1 - e^{-k_p t}}{k_p} \sup_{0\le\tau\le t} |e_2(\tau)|. \tag{61}$$

Since $\|e_{2,k}\|_\infty \le \varepsilon_{\text{eso}}$ and $k_p > 0$, letting $t \to \infty$ gives

$$\limsup_{t\to\infty} |e_\omega(t)| \le \frac{\varepsilon_{\text{eso}}}{k_p}. \tag{62}$$

Because $e_{\omega,k}(\vartheta) = e_\omega(kT_c + \vartheta)$, this result is equivalently expressed as

$$\limsup_{k\to\infty} \|e_{\omega,k}\|_\infty \le \frac{\varepsilon_{\text{eso}}}{k_p}, \tag{63}$$

which establishes (57). □

5. Experimental Verification

5.1. Experimental Setup

To validate the feasibility and effectiveness of the proposed control scheme, single-degree-of-freedom periodic angular-rate tracking experiments were conducted on the pitch axis of an inertially stabilized platform. Figure 4 shows the experimental platform and the hardware signal flow. The control algorithms were implemented on an STM32F407VET6 microcontroller. The computed control command was converted to an analog voltage by a 16-bit DAC8563 digital-to-analog converter (DAC) with an output range of ±5 V. The

resulting voltage was applied to a current drive module based on the OPA549, which drove the servo torque motor. The transconductance gain of the module was calibrated to 1 A/V.

The pitch axis angular velocity was measured by an AgileLight-320A fiber-optic gyroscope (FOG) and fed back to the microcontroller through an RS-422 interface. The gyroscope has an angle random walk coefficient of less than $0.01°/\sqrt{\text{h}}$. Its output was a 32-bit signed integer, which the microcontroller converted into an angular velocity value. The microcontroller was connected to a host computer for parameter tuning and experimental data acquisition. The control loop operated at 2 kHz, corresponding to a sampling period of T_s = 0.5 ms. All algorithms were evaluated using the same hardware platform, control frequency, sensor feedback, and current limit of 1 A, ensuring consistent comparison conditions.

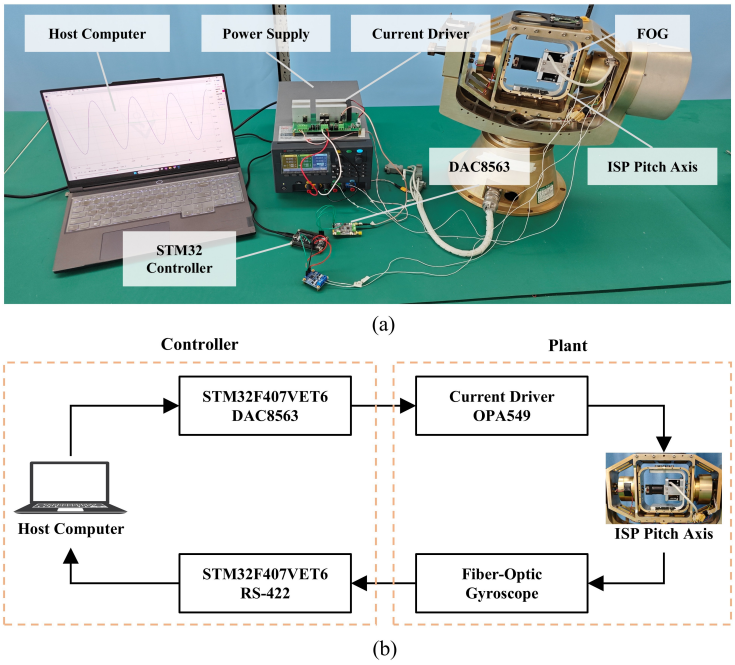


Figure 4. Experimental setup: (**a**) Experimental platform. (**b**) System hardware signal flow.

5.2. Experimental Design

A progressive comparison was performed using four control schemes: conventional linear active disturbance rejection control (LADRC) [26], conventional LADRC combined with ILC (LADRC+ILC) [42], a linear scheme with iterative learning embedded in the ESO disturbance estimation channel (IL-ESO), and the IL-FTESO defined in (20).

LADRC served as the baseline, while LADRC+ILC was used to assess the compensation provided by external iterative learning. IL-ESO retained the linear observer bandwidth of LADRC but embedded iterative learning in the disturbance estimation channel, allowing the effect of the embedded learning structure to be evaluated. IL-FTESO further incorporated a finite-time nonlinear correction mechanism to improve the disturbance estimation response and tracking performance near velocity reversals. IL-ESO and IL-FTESO used the same learning law and feedback control law, ensuring consistency in their embedded learning mechanisms and velocity feedback structures. The IL-ESO structure is defined as

$$\begin{cases} \dot{\hat{\omega}}_k = b_0 u_k + \hat{f}_{r,k}(\vartheta) + \hat{f}_{p,k} + \beta_1(\omega_k - \hat{\omega}_k), \\ \dot{\hat{f}}_{p,k} = \beta_2(\omega_k - \hat{\omega}_k), \\ \hat{f}_{r,k+1}(\vartheta) = Q_f\left[\hat{f}_{r,k}(\vartheta) + \gamma_d \hat{f}_{p,k}(\vartheta)\right]. \end{cases} \tag{64}$$

5.3. Parameter Selection and Digital Implementation

The control parameters of the four algorithms are listed in Table 1. The parameter selection considers the nominal plant gain, closed-loop response, observer dynamics, and iterative-learning convergence.

Table 1. Control parameters.

Symbol	Description	Value
b_0	Nominal control gain	8500
k_p	Feedback gain	125
ω_o	LESO bandwidth	380 rad/s
β_1, β_2	LESO gains	760 s^{-1}, 144,400 s^{-2}
ζ_1, ζ_2	FTESO gains	450 s^{-1}, 50,500 s^{-2}
λ	FTESO nonlinear parameter	1 $(^\circ/s)^{1/2}$
γ_p, Q_p	External ILC parameters	1.2×10^1, 0.985
γ_d, Q_f	Embedded ILC parameters	1.5×10^{-1}, 0.985

The nominal control gain b_0 was set to 8500 based on the frequency-response identification results. A linear proportional feedback controller was adopted because it yields exponentially stable nominal tracking-error dynamics while retaining a simple structure for disturbance compensation. To ensure a fair comparison, all four schemes used the same feedback structure and the same gain $k_p = 125$, so that their performance differences could be attributed to the disturbance-estimation and iterative-learning mechanisms rather than to changes in the feedback control law. LADRC, LADRC+ILC, and IL-ESO also used the same LESO bandwidth $\omega_o = 380$ rad/s. According to (15), the corresponding observer gains were set to $\beta_1 = 2\omega_o$ and $\beta_2 = \omega_o^2$. Since k_p was approximately $\omega_o/3$, the observer dynamics were faster than the closed-loop tracking dynamics. For the FTESO, $\lambda = 1$ was selected to balance the fractional-power and linear correction terms. The values of ζ_1 and ζ_2 were set below the corresponding LESO gains to balance disturbance-estimation speed against estimation chattering and high-frequency measurement-noise amplification.

The numerical feasibility of the sufficient conditions in Theorem 1 was examined using the experimental FTESO gains. For an assumed residual-disturbance rate bound of $D = 40\ ^\circ/s^3$, the scalar condition $\zeta_2\lambda^2/2 = 25250 > D$ is satisfied, and the LMI in (33) admits the feasible solution

$$P = \begin{bmatrix} 1.1545914 \times 10^4 & -96.81677 \\ -96.81677 & 1 \end{bmatrix}, \qquad \kappa = 0.01, \qquad \mu = 0.0207209.$$

For this solution, $\lambda_{\min}(P) = 0.1881 > 0$, and the maximum eigenvalue of the LMI matrix is $-2.62 \times 10^{-3} < 0$. Therefore, if Assumption 1 holds with $D \leq 40\ ^\circ/s^3$ over the continuous intervals between the bounded reversal-induced jumps, the experimental FTESO gains satisfy the sufficient numerical conditions of Theorem 1. This calculation establishes conditional feasibility for the specified disturbance class and does not constitute an independent experimental verification of Assumption 1.

The external ILC uses the angular-rate tracking error as its learning signal, whereas the embedded ILC uses the residual disturbance estimate. Because γ_p and γ_d act on signals with different physical meanings and units, their numerical values are not directly comparable and were tuned independently. The forgetting factors were both set to $Q_p = Q_f = 0.985$ to retain repetitive compensation while limiting the cycle-to-cycle accumulation of nonrepetitive components. The embedded ILC parameters were also selected to satisfy the contraction condition $\rho_L < 1$ in (50).

The iterative-learning compensation was implemented using a lookup table synchronized with each command cycle. At a control frequency of 2 kHz, the 0.5 Hz and 2 Hz commands required learning tables containing 4000 and 1000 samples per cycle, respectively. At each sampling instant, the STM32 retrieved the compensation value according to the corresponding time index within the cycle. The learning table was updated pointwise after each cycle. Both ILC schemes used the same cycle-synchronization procedure. To prevent startup transients from entering the learning table, only feedback control and real-time disturbance estimation were performed during the first cycle. Iterative learning was enabled from the second cycle onward.

5.4. Experimental Results

Three test cases were designed to evaluate the transient disturbance rejection performance of the FTESO and the periodic tracking performance of the IL-FTESO scheme separately. In Case 1, iterative learning was disabled to isolate the FTESO performance under a step angular-rate command, an external disturbance, and parameter variations. Case 2 used a cosine angular-rate command with an amplitude of 20°/s and a frequency of 0.5 Hz. Case 3 used a cosine angular-rate command with an amplitude of 5°/s and a frequency of 2 Hz. These cases evaluated the periodic tracking accuracy and iterative convergence of the proposed method under different combinations of command amplitude and frequency.

The analyses of Cases 2 and 3 were based on experimental data from five consecutive steady-state cycles after iterative convergence. The root–mean–square error (RMSE), maximum absolute error (MAXE), and mean absolute error (MAE) were used to quantify the periodic tracking performance of each algorithm and are defined as

$$\begin{aligned} \mathrm{RMSE} &= \sqrt{\frac{1}{N_s}\sum_{i=1}^{N_s} e_\omega^2(i)}, \\ \mathrm{MAXE} &= \max_{1\le i\le N_s} |e_\omega(i)|, \\ \mathrm{MAE} &= \frac{1}{N_s}\sum_{i=1}^{N_s} |e_\omega(i)|. \end{aligned} \tag{65}$$

Here, $e_\omega(i) = \omega_{\mathrm{ref}}(i) - \omega(i)$ is the angular-rate tracking error at the ith sampling instant, and N_s is the total number of samples collected over the five consecutive steady-state cycles.

5.4.1. Case 1: Step Tracking, Disturbance Rejection, and Parameter Robustness of the FTESO

To evaluate the dynamic response and robustness of the FTESO independently of iterative learning, ILC was disabled and the FTESO was compared with the conventional LESO. At t = 0.5 s, a step angular-rate command with an amplitude of 5°/s was applied. For Case 1, the derivative term $\dot{\omega}_{\mathrm{ref},k}$ in (26) was generated using the following second-order linear tracking differentiator:

$$\begin{cases} \dot{x}_1 = x_2, \\ \dot{x}_2 = -\omega_n^2(x_1 - \omega_{\mathrm{ref},k}) - 2\zeta\omega_n x_2, \end{cases} \tag{66}$$

where $\zeta = 0.707$, $\omega_n = 2\pi \times 20$ rad/s, and x_2 was used in place of $\dot{\omega}_{\mathrm{ref},k}$ in the control law. Thus, the ideal step command was not differentiated directly. After the system reached steady state, an independent 0.036 V step signal was superimposed through the DAC channel at $t = 2.0$ s to emulate an equivalent torque disturbance in the input channel. The observer continued to use the control input without the superimposed signal. At $t = 3.0$ s,

the nominal control gain used by the controller was changed from b_0 to $1.2b_0$, introducing a control gain mismatch.

Figure 5 compares the velocity responses obtained with the two observers. During step command tracking, the FTESO responded faster than the LESO. Following the disturbance applied at t = 2.0 s, the minimum velocities obtained with the LESO and FTESO were 4.06°/s and 4.45°/s, respectively. The corresponding maximum velocity drops were 0.94°/s and 0.55°/s, indicating a reduction of 41.5% with the FTESO. After the control gain change at t = 3.0 s, the peak velocities obtained with the LESO and FTESO were 5.38°/s and 5.17°/s, respectively. The corresponding maximum velocity deviations were 0.38°/s and 0.17°/s, representing a reduction of 55.3% with the FTESO. The FTESO also exhibited shorter recovery times following both perturbations.

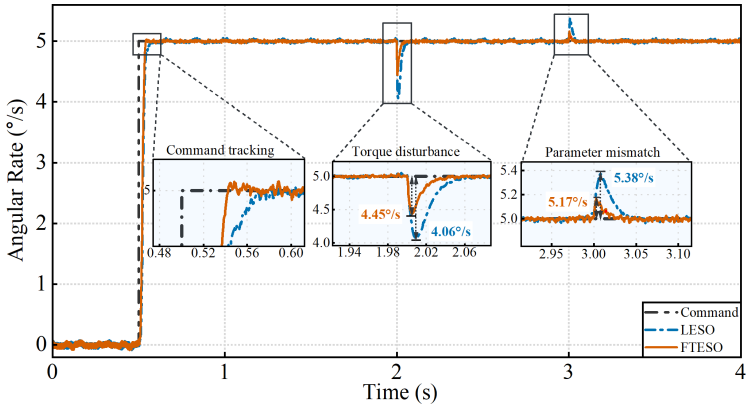


Figure 5. Dynamic responses of the LESO and FTESO under command tracking, torque disturbance, and parameter mismatch.

These results show that the FTESO reduced transient velocity deviations and shortened the subsequent recovery time under a step input disturbance and control gain mismatch compared with the LESO.

5.4.2. Case 2: Periodic Angular-Rate Tracking at 20°/s and 0.5 Hz

Figure 6 presents the time-domain experimental results obtained with the four algorithms after iterative convergence. As shown in Figure 6a, conventional LADRC exhibited a noticeable tracking deviation near the velocity peaks. All three iterative learning algorithms reduced this deviation, with IL-FTESO tracking the reference most closely. Figure 6b shows that the dominant error peaks of all four algorithms occurred near zero velocity reversals. LADRC produced the largest transient errors, whereas iterative learning reduced the reversal errors, with IL-FTESO yielding the smallest peaks.

The disturbance compensation quantities generated by the four algorithms are shown in Figure 6c. For a consistent comparison, the disturbance-compensation signals are expressed as equivalent voltages: $\hat{f}_k/b_0$ in (17) for LADRC and LADRC+ILC, and $u_{d,k}$ in (27) for IL-ESO and IL-FTESO. Near zero velocity reversals, all three iterative learning algorithms used information from the preceding cycle to adjust the compensation before the reversal error peaks occurred. Compared with external LADRC+ILC, IL-ESO and IL-FTESO updated their periodic compensation tables using observer disturbance estimates and initiated the compensation action earlier. IL-FTESO produced the earliest compensation response. This anticipatory action was also reflected in the actual control input shown in Figure 6d, which began to adjust before each velocity reversal. The control inputs of all four algorithms remained within the actuator limits, and no saturation occurred.

The steady-state tracking metrics after iterative convergence are reported in Table 2. IL-FTESO achieved the lowest RMSE, MAXE, and MAE among the four algorithms. Relative

to LADRC, LADRC+ILC, and IL-ESO, IL-FTESO reduced the RMSE by approximately 81.4%, 58.8%, and 36.6%, respectively. Relative to IL-ESO, which used the same embedded learning structure, IL-FTESO reduced the MAXE and MAE by approximately 30.0% and 29.4%, respectively. These results show that the proposed method reduced the peak errors near zero velocity reversals while also decreasing the overall tracking error.

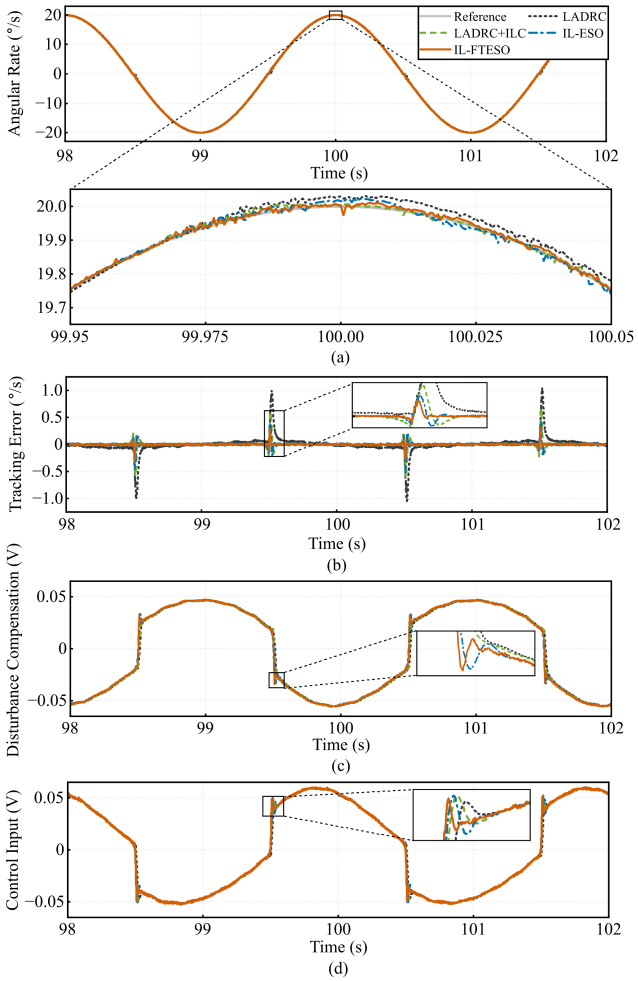


Figure 6. Experimental results under a 20°/s, 0.5 Hz cosine angular-rate command. (**a**) Angular-rate tracking results and enlarged view near the peak. (**b**) Tracking error. (**c**) Disturbance compensation voltage. (**d**) Control input voltage.

Table 2. Steady-state tracking error metrics under a 20°/s, 0.5 Hz cosine angular-rate command.

Method	RMSE (°/s)	MAXE (°/s)	MAE (°/s)
LADRC	0.1443	1.0718	0.0624
LADRC+ILC	0.0651	0.6713	0.0192
IL-ESO	0.0423	0.5237	0.0126
IL-FTESO	**0.0268**	**0.3665**	**0.0089**

Note: The best results among the compared methods are shown in bold.

Figure 7 presents the cycle-by-cycle RMSE convergence curves of the four algorithms. Convergence was considered achieved when the RMSE variation over five consecutive cycles was less than 5% of the steady-state value. Without iterative learning, the RMSE of LADRC remained at approximately 0.1443°/s. LADRC+ILC, IL-ESO, and IL-FTESO converged after 26, 47, and 41 cycles, respectively, with corresponding steady-state RMSE values of 0.0651°/s, 0.0423°/s, and 0.0268°/s. Although IL-FTESO converged more slowly

than LADRC+ILC, it achieved a lower steady-state RMSE. Relative to IL-ESO, IL-FTESO reduced the required number of cycles by approximately 12.8% and the steady-state RMSE by approximately 36.6%.

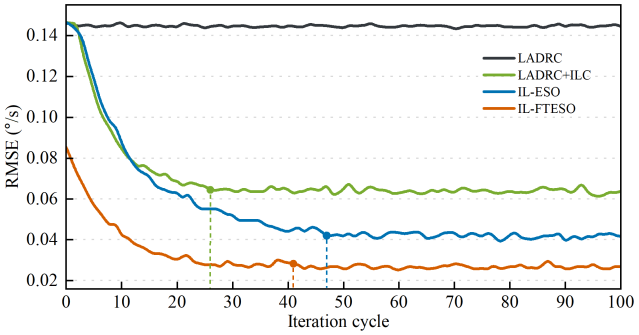


Figure 7. RMSE convergence under a 20°/s, 0.5 Hz cosine angular-rate command.

During periodic reciprocating motion, the nonlinear friction disturbance associated with velocity reversals changes direction between adjacent half-cycles and therefore exhibits approximate half-wave antisymmetry. Its spectrum typically contains pronounced odd harmonics. To assess the suppression of periodic errors associated with velocity reversals, a fast Fourier transform (FFT) was applied to the tracking error at steady state. Error amplitudes were extracted at the fundamental frequency and the third, fifth, and seventh harmonics, corresponding to 0.5 Hz, 1.5 Hz, 2.5 Hz, and 3.5 Hz, respectively. The results are presented in Figure 8. All three iterative learning algorithms reduced the error amplitudes at these frequencies relative to LADRC. IL-ESO and IL-FTESO produced lower amplitudes than external LADRC+ILC, while IL-FTESO achieved the lowest amplitude at every examined frequency. This frequency-domain result is consistent with the time-domain error analysis and the steady-state metrics, indicating that the proposed method further suppressed the periodic tracking errors associated with velocity reversals.

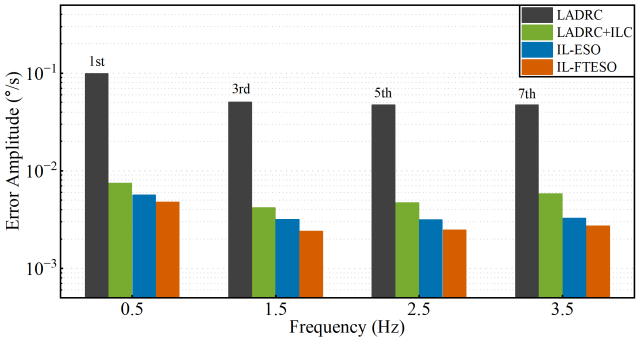


Figure 8. Harmonic amplitudes of the steady-state tracking error under a 20°/s, 0.5 Hz cosine angular-rate command.

5.4.3. Case 3: Periodic Angular-Rate Tracking at 5°/s and 2 Hz

In Case 3, the frequency of the cosine angular-rate command was increased from 0.5 Hz in Case 2 to 2 Hz, while its amplitude was reduced from 20°/s to 5°/s. This case evaluated periodic tracking performance under more frequent velocity reversals. Figure 9 shows the time-domain experimental results for the four algorithms after iterative convergence.

As shown in Figure 9a,b, LADRC exhibited noticeable tracking lag and amplitude deviations near the velocity peaks, with its error peaks concentrated primarily near zero velocity reversals. Both LADRC+ILC and IL-ESO reduced the tracking error after iterative learning was introduced. Among the four algorithms, the IL-FTESO response most closely followed the reference command and produced the smallest error peaks near the reversals.

Figure 9c,d further show that IL-FTESO initiated its compensation action earlier near zero velocity reversals. This anticipatory compensation was also evident in the actual control input. The control inputs of all four algorithms remained within the actuator limits, and no saturation occurred.

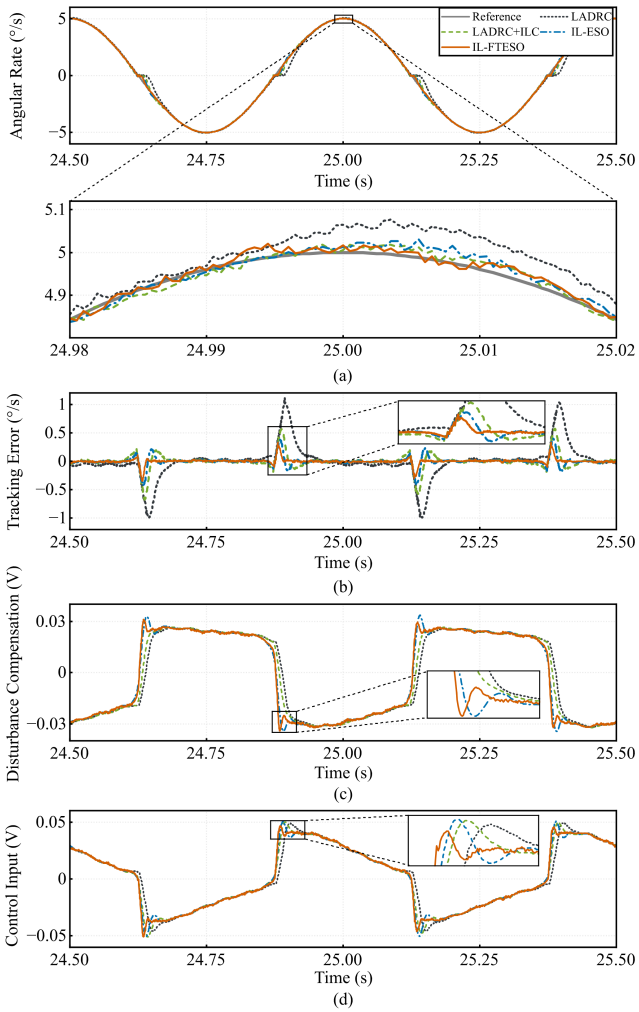


Figure 9. Experimental results under a 5°/s, 2 Hz cosine angular-rate command. (**a**) Angular-rate tracking results and enlarged view near the peak. (**b**) Tracking error. (**c**) Disturbance compensation voltage. (**d**) Control input voltage.

Table 3 reports the steady-state tracking metrics. Compared with Case 2, all four algorithms exhibited higher RMSE values despite the lower command amplitude, suggesting that the more frequent velocity reversals made dynamic tracking more demanding. IL-FTESO achieved the lowest RMSE, MAXE, and MAE among the four algorithms. Relative to LADRC, LADRC+ILC, and IL-ESO, IL-FTESO reduced the RMSE by approximately 81.9%, 61.0%, and 39.9%, respectively. Relative to IL-ESO, which used the same embedded learning structure, IL-FTESO reduced the MAXE and MAE by approximately 20.9% and 48.0%, respectively. These results show that the proposed method reduced the peak errors and improved the overall tracking accuracy under more frequent velocity reversals.

Figure 10 presents the cycle-by-cycle RMSE convergence curves of the four algorithms. Because LADRC did not incorporate iterative learning, its RMSE showed no downward trend over successive cycles. According to the convergence criterion defined above, LADRC+ILC, IL-ESO, and IL-FTESO converged after 22, 48, and 27 cycles, respectively, with corresponding steady-state RMSE values of 0.1291°/s, 0.0837°/s, and 0.0503°/s. Although IL-FTESO required more cycles to converge than LADRC+ILC, it achieved a

lower steady-state RMSE. Relative to IL-ESO, IL-FTESO reduced the number of cycles required for convergence from 48 to 27 while further decreasing the steady-state error.

Table 3. Steady-state tracking error metrics under a 5°/s, 2 Hz cosine angular-rate command.

Method	RMSE (°/s)	MAXE (°/s)	MAE (°/s)
LADRC	0.2786	1.1183	0.1405
LADRC+ILC	0.1291	0.6693	0.0629
IL-ESO	0.0837	0.4386	0.0381
IL-FTESO	**0.0503**	**0.3471**	**0.0198**

Note: The best results among the compared methods are shown in bold.

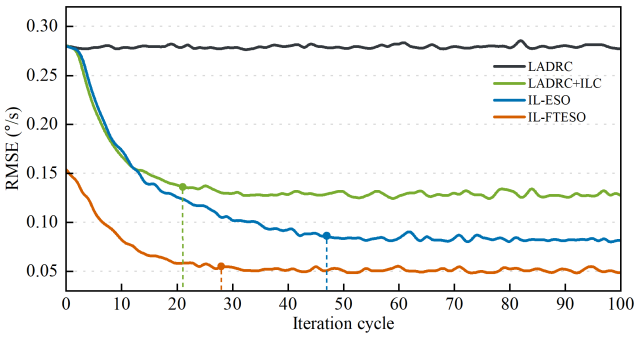


Figure 10. RMSE convergence under a 5°/s, 2 Hz cosine angular-rate command.

The steady-state tracking error was analyzed using the same FFT method as in Case 2, and the results are shown in Figure 11. All three iterative learning algorithms reduced the error amplitudes at the fundamental frequency and the dominant odd harmonics relative to LADRC. IL-ESO and IL-FTESO produced lower amplitudes than external LADRC+ILC, while IL-FTESO achieved the lowest amplitude at every frequency examined. This frequency-domain result agrees with the time-domain analysis, indicating that the proposed method also suppressed periodic tracking errors associated with velocity reversals under the 2 Hz angular-rate command.

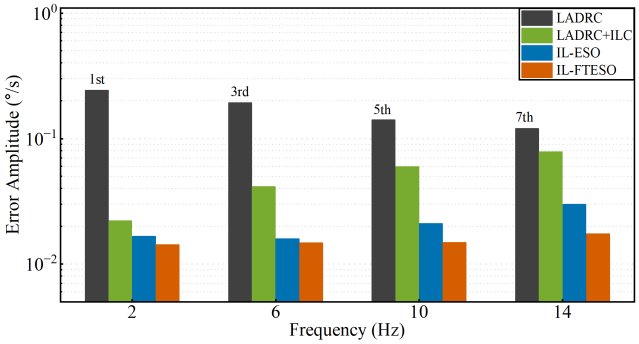


Figure 11. Harmonic amplitudes of the steady-state tracking error under a 5°/s, 2 Hz cosine angular-rate command.

6. Conclusions

This study developed an IL-FTESO disturbance rejection method for periodic angular-rate tracking of an inertially stabilized platform. The proposed scheme embeds ILC in the disturbance estimation channel and uses FTESO disturbance estimates, rather than tracking errors, as the learning signal. This design links real-time disturbance observation within each cycle to cycle-to-cycle compensation updates. The stability analysis establishes the convergence of the FTESO observation error and the ultimate boundedness of both the

learning error and the closed-loop tracking error. Tests on the physical platform verified that the FTESO improved transient recovery under a step disturbance and control-gain mismatch. Compared with conventional external ILC, IL-FTESO reduced the angular-rate tracking RMSE, MAXE, and MAE by at least 58.8%, 45.4%, and 53.6%, respectively. These results demonstrate the practical advantage of the proposed architecture for periodic scanning tasks.

The experimental validation focused on a single pitch axis under fixed periodic commands. Future work will incorporate online trajectory identification to handle changing trajectories. Adaptive learning updates will also be explored to cope with more complex disturbances.

Author Contributions: Conceptualization, C.Y., H.S. and H.C.; methodology, C.Y.; software, C.Y. and Y.X.; validation, C.Y., H.S. and Y.X.; writing—original draft preparation, C.Y. and C.L.; writing—review and editing, C.Y. and R.X.; supervision, H.C.; project administration, C.L.; funding acquisition, C.L. All authors have read and agreed to the published version of the manuscript.

Funding: This research was funded by the Jilin Provincial Science and Technology Development Program, grant number SKL202402023.

Data Availability Statement: The original contributions presented in this study are included in the article. Further inquiries can be directed to the corresponding author.

Conflicts of Interest: The authors declare no conflicts of interest.

References

1. Wen, T.; Xiang, B. The Airborne Inertially Stabilized Platform Suspend by an Axial-Radial Integrated Active Magnetic Actuator System. *J. Adv. Res.* **2021**, *31*, 191–205. [CrossRef]
2. Zheng, J.; Xie, X.; Li, B.; Wan, Z.; Chen, N.; Fan, D. Adaptive Multi-Parameter Estimation of Inertial Stabilization Platform with Unknown Load. *Actuators* **2023**, *12*, 176. [CrossRef]
3. Xu, K.; Xiao, M.; Xie, X.; Wen, Z.; Fan, S.; Fan, D. High-Precision Tracking Control of Multi-Axis Electro-Optical Systems Based on Accurate Identification of Dynamic Parameters. *IEEE Trans. Autom. Sci. Eng.* **2026**, *23*, 5516–5529. [CrossRef]
4. Yang, J.; Liu, X.; Sun, J.; Li, S. Sampled-Data Robust Visual Servoing Control for Moving Target Tracking of an Inertially Stabilized Platform with a Measurement Delay. *Automatica* **2022**, *137*, 110105. [CrossRef]
5. Qu, J.; Xia, Y.; Shi, Y.; Cao, J.; Wang, H.; Meng, Y. Modified ADRC for Inertial Stabilized Platform with Corrected Disturbance Compensation and Improved Speed Observer. *IEEE Access* **2020**, *8*, 157703–157716. [CrossRef]
6. Cui, Y.; Qiao, J.; Zhu, Y.; Yu, X.; Guo, L. Velocity-Tracking Control Based on Refined Disturbance Observer for Gimbal Servo System with Multiple Disturbances. *IEEE Trans. Ind. Electron.* **2022**, *69*, 10311–10321. [CrossRef]
7. Zhou, X.; Zhao, B.; Liu, W.; Yue, H.; Yu, R.; Zhao, Y. A Compound Scheme on Parameters Identification and Adaptive Compensation of Nonlinear Friction Disturbance for the Aerial Inertially Stabilized Platform. *ISA Trans.* **2017**, *67*, 293–305. [CrossRef]
8. Zhang, Z.; Li, Z.; Zhou, Q.; Zhang, L.; Fan, D. Application in Prestiction Friction Compensation for Angular Velocity Loop of Inertially Stabilized Platforms. *Chin. J. Aeronaut.* **2014**, *27*, 655–662. [CrossRef]
9. Wang, J.; Yang, T. Active Disturbance Rejection Control of Quadrotor UAVs Under Uncertainties and Disturbances. *Actuators* **2026**, *15*, 286. [CrossRef]
10. Zhou, X.; Wang, W.; Gao, H.; Shu, T.; Zhu, Z. Non-Model Friction Disturbance Compensation for an Inertially Stabilized Platform Based on Type-2 Fuzzy Control with Self-Adjusting Correction Factor. *Proc. Inst. Mech. Eng. Part C J. Mech. Eng. Sci.* **2023**, *237*, 2401–2412. [CrossRef]
11. Dong, F.; Lei, X.; Chou, W. A Dynamic Model and Control Method for a Two-Axis Inertially Stabilized Platform. *IEEE Trans. Ind. Electron.* **2017**, *64*, 432–439. [CrossRef]
12. Zhang, M.; Guan, Y.; Li, C.; Luo, S.; Li, Q. Backstepping Control for the Optoelectronic Stabilized Platform Based on Adaptive Fuzzy Logic System and Nonlinear Disturbance Observer. *Nonlinear Dyn.* **2023**, *111*, 8347–8368. [CrossRef]
13. Bian, Q.; Miao, Q.; Yu, Z.; Tang, T.; Ma, H. Nonlinear Acceleration Disturbance Observer to Reject Transient Peak Disturbances for an Inertial Stabilization-Tracking Platform. *ISA Trans.* **2025**, *160*, 237–247. [CrossRef]
14. Zhang, Y.; Yang, T.; Li, C.; Liu, S.; Du, C.; Li, M.; Sun, H. Fuzzy-PID Control for the Position Loop of Aerial Inertially Stabilized Platform. *Aerosp. Sci. Technol.* **2014**, *36*, 21–26. [CrossRef]

15. Zhou, X.; Wang, W.; Shi, Y. Neural Network/PID Adaptive Compound Control Based on RBFNN Identification Modeling for an Aerial Inertially Stabilized Platform. *IEEE Trans. Ind. Electron.* **2024**, *71*, 16514–16522. [CrossRef]
16. Mao, J.; Yang, J.; Liu, X.; Li, S.; Li, Q. Modeling and Robust Continuous TSM Control for an Inertially Stabilized Platform With Couplings. *IEEE Trans. Control Syst. Technol.* **2020**, *28*, 2548–2555. [CrossRef]
17. Wang, Y.; Yang, Y.; Kuang, H.; Yuan, D.; Yu, C.; Chen, J.; Hua, N.; Hou, H. High Performance Both in Low-Speed Tracking and Large-Angle Swing Scanning Based on Adaptive Nonsingular Fast Terminal Sliding Mode Control for a Three-Axis Universal Inertially Stabilized Platform. *Sensors* **2020**, *20*, 5785. [CrossRef]
18. Ding, W.; Yu, Z.; Miao, Q.; Bian, Q.; Tang, T. Nonlinear High-Frequency Dynamics Rejection of Disturbance Observed Sliding Mode Control for Inertially Stabilized Gimbal. *Control Eng. Pract.* **2026**, *168*, 106697. [CrossRef]
19. Zhang, Y.; Cao, S.; Shi, Y.; Yu, Y. High-Dynamic Composite Control Based on IDNTSMC and FTESO for Gimbal Servo System. *IEEE Trans. Ind. Electron.* **2026**, *73*, 12351–12362. [CrossRef]
20. Deng, K.; Cong, S.; Kong, D.; Shen, H. Discrete-Time Direct Model Reference Adaptive Control Application in a High-Precision Inertially Stabilized Platform. *IEEE Trans. Ind. Electron.* **2019**, *66*, 358–367. [CrossRef]
21. Qiu, G.; Hao, Y.; Chen, G.; Yan, G.; Chen, Y. Adaptive Backstepping Control for Battery Pole Strip Mill Systems with Friction and Dead-Zone Input Nonlinearities. *Actuators* **2025**, *14*, 618. [CrossRef]
22. Sui, S.; Yao, Y.; Zhao, T. Multi-Degree-of-Freedom Internal Model Control for Optoelectronic Stabilized Platform Based on Sliding Mode Friction Compensation. *Int. J. Control Autom. Syst.* **2023**, *21*, 3994–4005. [CrossRef]
23. Sariyildiz, E.; Oboe, R.; Ohnishi, K. Disturbance Observer-Based Robust Control and Its Applications: 35th Anniversary Overview. *IEEE Trans. Ind. Electron.* **2020**, *67*, 2042–2053. [CrossRef]
24. Yang, Y.; Cui, Y.; Qiao, J.; Zhu, Y. Adaptive Periodic-Disturbance Observer Based Composite Control for SGCMG Gimbal Servo System with Rotor Vibration. *Control Eng. Pract.* **2023**, *132*, 105407. [CrossRef]
25. Liu, K.; Li, T.; Lu, R.; Wang, Y.; Jia, C.; Zhao, P. Disturbance Observer-Based Adaptive Predefined-Time Attitude Control for Tiltrotor UAVs With Actuator Faults. *IEEE Trans. Aerosp. Electron. Syst.* **2026**, *62*, 9258–9282. [CrossRef]
26. Gao, Z. Scaling and Bandwidth-Parameterization Based Controller Tuning. In *Proceedings of the 2003 American Control Conference, 2003*; IEEE: Piscataway, NJ, USA, 2003; Volume 6, pp. 4989–4996. [CrossRef]
27. Han, J. From PID to Active Disturbance Rejection Control. *IEEE Trans. Ind. Electron.* **2009**, *56*, 900–906. [CrossRef]
28. Shi, W.; Liu, K.; Zhao, W. Active Vibration Isolation of a Maglev Inertially Stabilized Platform Based on an Improved Linear Extended State Observer. *IEEE Access* **2021**, *9*, 743–751. [CrossRef]
29. Shi, Y.; Li, H.; Han, B. Position Extraction of Ultralow-Speed Gimbal Servo System with Linear Hall Sensors. *IEEE Trans. Ind. Electron.* **2022**, *69*, 2947–2955. [CrossRef]
30. Wang, L.; Zhang, L.; Meng, L.; Bai, Y. Research on Cooperative Stabilization Control of Multi-Pointing-Mirror Laser Communication Terminals Based on GA-ADRC. *Actuators* **2025**, *14*, 571. [CrossRef]
31. Cao, H.; Deng, Y.; Zuo, Y.; Li, H.; Wang, J.; Liu, X.; Lee, C.H.T. Improved ADRC with a Cascade Extended State Observer Based on Quasi-Generalized Integrator for PMSM Current Disturbances Attenuation. *IEEE Trans. Transp. Electrif.* **2024**, *10*, 2145–2157. [CrossRef]
32. Hou, Q.; Zuo, Y.; Sun, J.; Lee, C.H.T.; Wang, Y.; Ding, S. Modified Nonlinear Active Disturbance Rejection Control for PMSM Speed Regulation with Frequency Domain Analysis. *IEEE Trans. Power Electron.* **2023**, *38*, 8126–8134. [CrossRef]
33. Liu, X.; Deng, Y.; Cao, H.; Wang, J.; Li, H.; Lee, C.H.T. Modified ADRC Based on Quasi-Resonant Fixed-Time-Convergent Extended State Observer for PMSM Current Regulation. *IEEE Trans. Transp. Electrif.* **2025**, *11*, 1416–1430. [CrossRef]
34. Ye, D.; Zou, A.M.; Sun, S.; Xiao, Y. A Predefined-Time Extended-State Observer-Based Approach for Velocity-Free Attitude Control of Spacecraft. *IEEE Trans. Aerosp. Electron. Syst.* **2023**, *59*, 8051–8061. [CrossRef]
35. Zhang, Z.; Guo, Y.; Zhu, S.; Ji, P.; Jiao, F.; Song, X.; Gong, D. Adaptive Nonlinear ESO-Based Global Sliding-Mode Control of EV-PMSM With Unmeasurable Disturbance. *IEEE Trans. Instrum. Meas.* **2026**, *75*, 3000613. [CrossRef]
36. Łakomy, K.; Madonski, R. Cascade Extended State Observer for Active Disturbance Rejection Control Applications under Measurement Noise. *ISA Trans.* **2021**, *109*, 1–10. [CrossRef]
37. Yang, L.; Liu, L.; Zhang, J. A Bi-Bandwidth Extended State Observer for a System with Measurement Noise and Its Application to Aircraft with Abrupt Structural Damage. *Aerosp. Sci. Technol.* **2021**, *114*, 106742. [CrossRef]
38. Zhai, C.; Deng, Y.; Cao, H.; Kang, Y.; Li, W.; Xu, L.; Liu, X.; Lee, C.H.T. Enhanced ADRC with an Improved Extended State Observer Considering Aperiodic and Periodic Disturbances for PMSM Drives. *IEEE Trans. Ind. Electron.* **2026**, *73*, 3758–3769. [CrossRef]
39. Du, C.; Ke, Z.; Yin, Z.; Qiu, L.; Ma, J.; Niu, F.; Fang, Y.; Rodriguez, J. A Cascaded Current Harmonics Suppression Method Considering Steady-State and Dynamic Characteristics for PMSM Based on Quasi-Resonant Extended State Observer. *IEEE Trans. Transp. Electrif.* **2026**, *12*, 4528–4543. [CrossRef]
40. Yang, X.; Hu, H.; Hu, H.; Liu, Y.; He, Z. A Quasi-Resonant Extended State Observer-Based Predictive Current Control Strategy for Three-Phase PWM Rectifier. *IEEE Trans. Ind. Electron.* **2022**, *69*, 13910–13917. [CrossRef]

41. Saab, S.S.; Shen, D.; Orabi, M.; Kors, D.; Jaafar, R.H. Iterative Learning Control: Practical Implementation and Automation. *IEEE Trans. Ind. Electron.* **2022**, *69*, 1858–1866. [CrossRef]
42. Huang, D.; Min, D.; Jian, Y.; Li, Y. Current-Cycle Iterative Learning Control for High-Precision Position Tracking of Piezoelectric Actuator System via Active Disturbance Rejection Control for Hysteresis Compensation. *IEEE Trans. Ind. Electron.* **2020**, *67*, 8680–8690. [CrossRef]
43. Zhang, G.; Zhao, X.; Wang, Q.; Ding, D.; Li, B.; Wang, G.; Xu, D. PR Internal Mode Extended State Observer-Based Iterative Learning Control for Thrust Ripple Suppression of PMLSM Drives. *IEEE Trans. Power Electron.* **2024**, *39*, 10095–10105. [CrossRef]
44. Wang, S.; Chen, J.; He, X. An Adaptive Composite Disturbance Rejection for Attitude Control of the Agricultural Quadrotor UAV. *ISA Trans.* **2022**, *129*, 564–579. [CrossRef]
45. Meng, D. Convergence Conditions for Solving Robust Iterative Learning Control Problems under Nonrepetitive Model Uncertainties. *IEEE Trans. Neural Netw. Learn. Syst.* **2019**, *30*, 1908–1919. [CrossRef]
46. Chi, R.; Hui, Y.; Chien, C.J.; Huang, B.; Hou, Z. Convergence Analysis of Sampled-Data ILC for Locally Lipschitz Continuous Nonlinear Nonaffine Systems with Nonrepetitive Uncertainties. *IEEE Trans. Autom. Control* **2021**, *66*, 3347–3354. [CrossRef]
47. Filippov, A.F. *Differential Equations with Discontinuous Righthand Sides*; Mathematics and Its Applications; Springer: Dordrecht, The Netherlands, 1988; Volume 18. [CrossRef]
48. Cortes, J. Discontinuous Dynamical Systems. *IEEE Control Syst. Mag.* **2008**, *28*, 36–73. [CrossRef]

Disclaimer/Publisher's Note: The statements, opinions and data contained in all publications are solely those of the individual author(s) and contributor(s) and not of MDPI and/or the editor(s). MDPI and/or the editor(s) disclaim responsibility for any injury to people or property resulting from any ideas, methods, instructions or products referred to in the content.